PHOTONICS Research

Ultrabroadband nonlinear Raman–Nath diffraction against femtosecond pulse laser

Lihong Hong,[1] Baoqin Chen,[1] Chenyang Hu,[2] and Zhi-Yuan Li[1,*]

[1]School of Physics and Optoelectronics, South China University of Technology, Guangzhou 510641, China
[2]Guangdong Jingqi Laser Technology Corporation Limited, Dongguan 523808, China
*Corresponding author: phzyli@scut.edu.cn

Received 23 November 2021; revised 6 February 2022; accepted 9 February 2022; posted 9 February 2022 (Doc. ID 449297); published 11 March 2022

Nonlinear Raman–Nath diffraction (NRND) offers an effective way to realize multiple noncollinear parametric processes based on the partially satisfied transverse phase-matching conditions in quadratic nonlinear media. Here, the realization of ultrabroadband NRND (UB-NRND) driven by a high-peak-power ultrashort femtosecond pump laser in two types of nonlinear crystals is reported: periodically poled lithium niobate (PPLN) and chirped PPLN (CPPLN). Multi-order ultrabroadband Raman–Nath second-harmonic (SH) signal outputs along fixed diffraction angles are simultaneously observed. This distinguished transversely phase-matched supercontinuum phenomenon is attributed to the synergic action of natural broad bandwidth of an ultrashort femtosecond pump laser and the third-order nonlinear effect induced spectral broadening, in combination with the principal ultrabroadband noncollinear second-harmonic generation processes. The NRND process with multiple quasi-phase matching (QPM) interactions from CPPLN leads to the SH output covering a wide range of wavelengths between 389 and 997 nm and exhibiting an energy conversion efficiency several orders of magnitude higher than previous studies. This UB-NRND scheme would bring better techniques and tools for applications ranging from ultrashort pulse characterization and nondestructive identification of domain structures to accurate parameter monitoring of second- and third-order nonlinear susceptibilities within solid-state nonlinear microstructured materials.

https://doi.org/10.1364/PRJ.449297

1. INTRODUCTION

Second-harmonic generation (SHG) is one of the most essential techniques to expand the laser wavelength range via either a birefringence phase matching (BPM) [1] or a quasi-phase-matching (QPM) scheme [2] in the engineered quadratic nonlinear photonics crystals with spatial modulation on the second-order nonlinearity $\chi^{(2)}$. Usually, efficient QPM processes are based on collinear light interactions [3–7]. As fascinating alternatives, various noncollinear physical phenomena, including nonlinear Bragg diffraction [8–10], nonlinear Raman–Nath diffraction (NRND) [11], and nonlinear Cerenkov diffraction [12–14], from various nonlinear microstructures, have raised extensive and intensive interest in physical study and optical applications. In these cases, the harmonics of the incident wave are the partially phase-matched emissions with the propagation direction of the fundamental pump beam perpendicular to the modulation direction of $\chi^{(2)}$ nonlinear microstructures. Particularly, the nonlinear Bragg diffraction and the NRND process present close nonlinear analogies to the well-known linear beam diffraction on a dielectric grating [15,16].

The NRND emission can in fact be looked upon as the optical parametric process satisfying transverse phase-matching because of the existence of a reciprocal lattice vector (RLV) in the transverse direction of $\chi^{(2)}$ nonlinear microstructures. This phenomenon was first discovered in an early work [11] and then expanded from typical 1D periodic nonlinear microstructures [17,18] to engineered 2D nonlinear photonic crystals [19,20]. It has then attracted increasing interest due to the relaxed phase-matching condition, and has enabled a wide tunability in the spectral and angular ranges of nonlinear optical interaction. Moreover, it provides a feasible tool that enables higher-order effects via the cascading effect of different Raman–Nath diffractions [21]. Great efforts involving both experimental investigations [22–25] and theoretical analysis [26,27] have been made to understand and optimize this nonlinear effect. Owing to the sensitivity of nonlinear diffraction to atomic-scale physical asymmetry in local area of nonlinear microstructures, deeper interest is focused on its comprehensive practical applications such as nondestructive diagnostics of domain structures [19,22,28–30], and the parameter test of periodically poled microstructures (e.g., period and duty cycle) [24,25].

However, to date, all previous studies have been largely restricted to the narrow bandwidth of the Raman–Nath SHG

process, where the parametric processes are performed in the regimes of a monochromatic wave or a narrowband input beam [21,22,28,31]. This consequently has limited practical applicability of NRND. Besides, a detailed exploration of noncollinear frequency doubling via the NRND scheme based on the pump of ultrashort femtosecond pulse laser has not yet, to the best of our knowledge, been deeply carried out. Considering this situation, in this paper we systematically study the process of Raman–Nath SHG upon pumping the periodically poled lithium niobate (PPLN) and chirped PPLN (CPPLN) by a high-peak-power ultrashort femtosecond laser. We present a general experimental observation of ultrabroadband multiorder SHG emissions simultaneously from PPLN and CPPLN crystals via the NRND mechanism, which has enabled conversion of a near-IR (NIR) high-peak-power ultrashort femtosecond laser pulse into multiple visible white laser beam outputs in various directions. We deeply analyze both the broadband spectral properties at multiple diffraction orders and their angular emission geometries. We believe these results have demonstrated novel prospects for spectral monitoring of femtosecond optical signals over the broad spectral range from the visible to the NIR regions by noncollinear Raman–Nath processes. Moreover, the developed ultrabroadband NRND (UB-NRND) scheme may provide a universally available high-precision nondestructive method to visualize and diagnose domain characteristics, perform domain design, and even allow for accurate measurements of quadratic and third-order nonlinearity tensors in domain wall regions inside microstructured quadratic nonlinear crystals.

2. RESULTS AND DISCUSSION

A. Nonlinear Optical Experiments

In the experiment, we use a z-cut PPLN thin plate sample with dimensions of 5 mm (x) × 20 mm (y) × 1 mm (z) and a z-cut CPPLN thin plate sample with dimensions of 6 mm (x) × 20 mm (y) × 0.5 mm (z) as the nonlinear media. The poling period of the PPLN sample is fixed at a value of 6.96 μm and that of CPPLN ranges from 24 to 14.8 μm with a mean value of 18.34 μm. Their second-order nonlinear susceptibilities $\chi^{(2)}$ are modulated along the transverse (y) axis. The poling period of the CPPLN crystal is given by $\Lambda(y) = \Lambda_0/[1 + (D_g\Lambda_0 y/2\pi)]$ along the propagation direction of the pump laser (denoted as $+y$), where $\Lambda_0 = 2\pi/\Delta k_0$ and D_g is the chirp date. The wavevector mismatch Δk_0 is defined for SHG at the fundamental wavelength of 1300 nm. The PPLN and CPPLN samples can be prepared via the standard electric poling technique [4–7,32–36]. Schematic diagrams of the PPLN and CPPLN samples are explicitly illustrated in Figs. 1(a) and 1(b). The RLV lines provided by the PPLN structure involve some sharp peaks with high Fourier coefficients, as shown in Fig. 1(c), which indicates that the PPLN structure can provide an original auxiliary RLV to efficiently compensate the Raman–Nath phase mismatching via a single QPM interaction. In comparison, the CPPLN structure can provide multiple effective RLV bands with sufficiently large bandwidths and high Fourier coefficients, as sketched in Fig. 1(d). These broad RLV bands of the CPPLN structure may enable a series

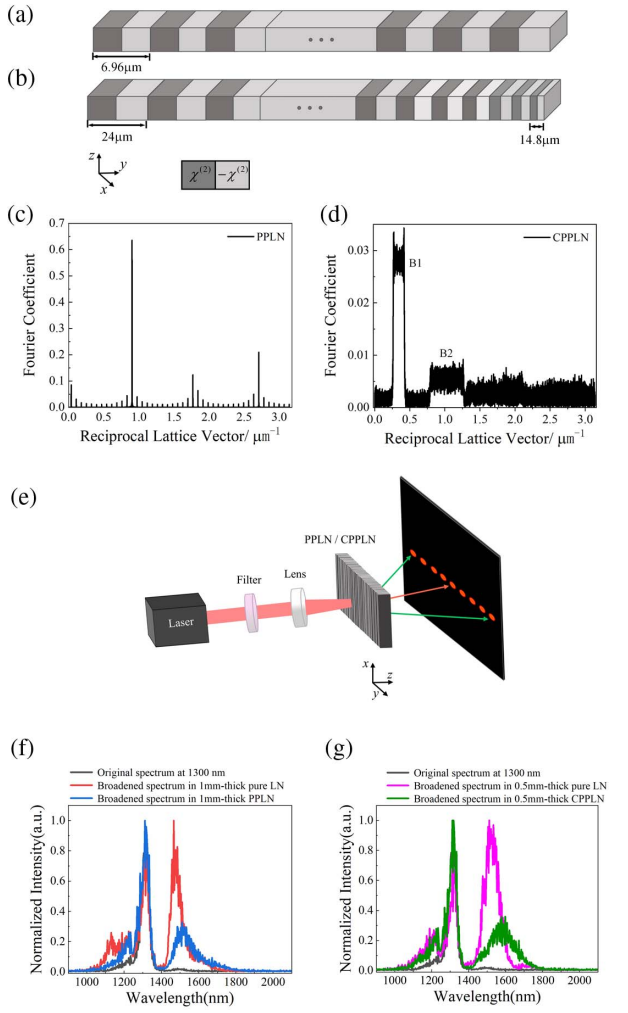

Fig. 1. Principle of NRND generation from the PPLN and CPPLN samples. (a), (b) Schematic diagram of the structural geometry of typical 1D PPLN and CPPLN structures. The poling period of the PPLN sample is 6.96 μm and that of the CPPLN crystal ranges from 24 to 14.8 μm. (c) Calculated distributions of the RLV lines in the PPLN structure. (d) The abundant multiple-band RLVs for the designed CPPLN sample. (e) Schematic experimental setup to study NRND. (f), (g) Original and broadened spectra for the pump laser pulse centered at 1300 nm passing through bare LN crystals with 1 mm and 0.5 mm in thickness, in correspondence to PPLN and CPPLN, respectively.

of cascaded QPM conditions in the transverse directions and yield multiple QPM-typed Raman–Nath diffraction patterns.

We measure and analyze the NRND processes from the PPLN and CPPLN samples using the apparatus shown in Fig. 1(e). The pump source is an NIR femtosecond laser at a central wavelength of 1300 nm with a pulse duration 50 fs, corresponding to a pulse FWHM of about 100 nm, a repetition rate of 1 kHz, a setting laser average power 60 mW, and an energy per pulse 60 μJ. The laser beam is weakly focused by an $f = 300$ mm fused silica lens with a spot radius of around 1 mm, coupled into the xy surface of the z-cut nonlinear crystal, and travels along the z axis (namely the thickness direction of LN thin plate) with a peak intensity

of 152 GW/cm^2. This power level is well below the optical damage threshold for these two samples. The pump and output laser spectra before and after the fundamental beam passes through bare LN crystals with 1 mm and 0.5 mm in thickness, corresponding to PPLN and CPPLN, respectively, are displayed in Figs. 1(f) and 1(g). Here, one can find that the output spectra in these nonlinear crystals all have significantly broadened bandwidths as high as ~200 nm, exhibiting a two times spectral broadening. Besides, the spectral broadening magnitudes for a bare LN crystal and microstructured PPLN and CPPLN crystals are almost the same. This indicates that the powerful third-order nonlinearity (3rd NL), including four-wave mixing, self-phase modulation (SPM), and stimulated Raman scattering, excited against the LN crystal by the high-energy-density pump laser has played an important role in such a noncollinear mechanism, very similar to the situation found in the collinear QPM case [37]. Additionally, one thing worth noting is that the lower sidebands of the pump broadening are significantly weaker in PPLN and CPPLN compared to the unpatterned ones, which might be due to the suppression of stimulated polariton scattering in periodically poled materials, similar to the physical mechanism in KTP [38]. To clarify the spectral property of the diffracted SHG laser, suitable filters are used to band-stop the pump laser and bandpass the output SHG signals. The generated Raman–Nath radiations are directly monitored by a regular camera (Nikon D7200) after they are projected on a screen placed 5.2 cm away from the output face of the crystal.

B. Ultrabroadband Emission Spectrum of Nonlinear Raman–Nath Diffraction

We first examine the PPLN sample. The observed Raman–Nath SHG patterns emitted from the PPLN sample with a regular period of 6.96 μm are displayed in Fig. 2(a). One can distinguish a series of ordered SH spots that correspond to the four nonlinear diffraction orders (left- and right-hand sides of the central spot) in the neighborhood of the passing fundamental laser spot. The multi-order Raman–Nath outputs

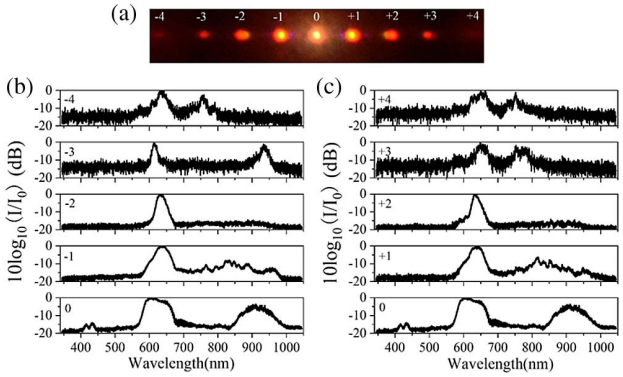

Fig. 2. Experimental results of NRND from the PPLN sample. (a) Experimentally recorded multi-order Raman–Nath diffraction patterns in engineered PPLN sample with 1300 nm femtosecond pump laser. (b), (c) Normalized broadband spectra of the Raman–Nath signals emitted from the PPLN sample at different diffraction orders as estimated by a criterion of −20 dB. Note that the spectrum in each panel has been normalized against the maximum value.

are observed with the eye-viewed color changing from bright white in the middle to faint red in the far end, which clearly indicates that the overall chroma of the output laser is changing as the diffraction order grows. Further on, we use an optical spectrometer to make an accurate spectral analysis over these output white light beams at different diffraction orders, and the results are illustrated in Figs. 2(b) and 2(c). Note that the spectrum in each panel has been normalized against the maximum value, and thus only shows the spectral profile but not the absolute intensity. One can find that the spectrum of the 0th diffraction beam exhibits colorful spectral components ranging from 400 to 998 nm, but is mainly concentrated in two modest bands of 550–697 nm and 831–998 nm. This can be ascribed to the direct nonphase-matched nonlinear process caused by high peak intensity of the input laser beam. As expected, the spectra of the Raman–Nath diffraction beams maintain coherent broadband spectral properties under the transversely phase-matched geometry. Interestingly, the diffracted lasers from the −1st order to −4th order (defined to be located in the left-hand side of the central spot) under the femtosecond laser pump with the central wavelength 1300 nm are found to involve a series of visible to NIR bands covering approximately 442–988 nm, 573–962 nm, 590–657 nm, 887–964 nm, and 565–807 nm, respectively, counted at a −20 dB intensity level. Similarly, the diffraction beams from the +1st order to +4th order (defined to be located in the right-hand side of the central spot) also have colorful bands covering 552–996 nm, 573–950 nm, 603–834 nm, and 611–796 nm, respectively.

Obviously, the overall spectrum of NRND beams emitted from the PPLN sample covers a series of visible white light bands ranging approximately from 442 to 988 nm, which is more evident in the first two diffraction orders; i.e., the 0th and 1st orders. A prominent feature indicative of ultrabroadband SH diffraction spectra is the five-times broadened bandwidth compared to the fundamental femtosecond pulse laser (slightly below 100 nm). We attribute this greatly enhanced broadband spectral property to the perfect synergy of effective Raman–Nath SH diffraction and significant third-order nonlinear effects induced by the high-peak-power pump laser. It should be noted that the NRND processes at higher diffraction orders are mainly the result of the second-order nonlinearity (2nd NL) effect with relatively lower conversion efficiencies; that is, the output spectra are more manifested in the central band approximately 600–800 nm at higher diffraction orders. This is why we see a gradual change in the chroma of the generated SH spots from the center to the left-hand side (or the right-hand side). Here, a pronounced spectral difference between the −3rd and +3rd orders in Figs. 2(b) and 2(c) may be due to the inhomogeneity of the domain structure or scattering effects from the crystal interfaces.

We proceed to investigate the CPPLN sample. The experimentally recorded 15 orders Raman–Nath diffraction emissions (ranging from the −7th order to +7th order) from the CPPLN sample, including the color pattern of SH laser spots and their normalized spectra, are exhaustively depicted in Fig. 3. It is obvious that more Raman–Nath spots with varying chromaticity can exit from the CPPLN sample due to the larger

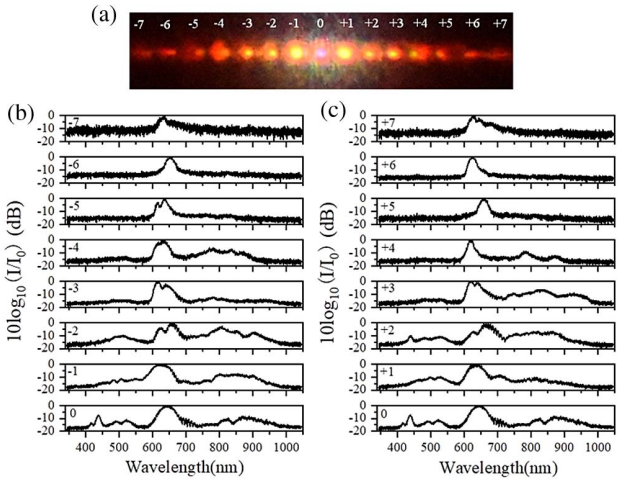

Fig. 3. Experimental results of NRND from the CPPLN sample. (a) Experimentally recorded multi-order Raman–Nath diffraction patterns in the engineered CPPLN sample with 1300 nm femtosecond pump laser. (b), (c) Normalized broadband spectra of the Raman–Nath signals emitted from the CPPLN sample at different diffraction orders as estimated by a criterion of −20 dB. Note that the spectrum in each panel has been normalized against the maximum value.

poling period compared with the PPLN sample. In the same manner, the wavelength range of the direct 0th SH light signal locates at a continuous band 400–998 nm, as clearly illustrated in the bottom rows of Figs. 3(b) and 3(c). The diffracted lasers from the −1st order to −7th order (defined to be located in the left-hand side of the central spot) encompass a sequence of broadband frequency domains at least of 389–997 nm, 395–995 nm, 458–976 nm, 466–940 nm, 589–847 nm, 604–713 nm, and 610–698 nm, respectively. Additionally, the spectral bands of the diffracted lasers from the +1st order to +7th order (defined to be located in the right-hand side of the central spot) are observed with a series of supercontinuum bands of 389–970 nm, 391–985 nm, 463–982 nm, 588–901 nm, 607–717 nm, 600–690 nm, and 605–703 nm, respectively. In brief, the measured overall spectrum of NRND output lasers emitted from the CPPLN crystal is composed of a supercontinuum, coherent white laser with wavelength mapping approximately from 389 to 997 nm, which is more evident in the first four diffraction orders; i.e., the 0th to 4th orders. Obviously, the CPPLN sample shows better broadening characteristics and multichannel supercontinuum white light signal outputs than the PPLN sample. It is clear that the chirped QPM structures that exhibit broadband RLVs can hugely expand the wavelength ranges of the emitted laser spectrum combined with the synergic action of ultrabroadband 2nd NL and 3rd NL interactions and result in the prominent phenomenon of ultrabroadband NRND. Thus, this approach can be named the QPM-UB-NRND scheme. To the best of our knowledge, this unique ultrabroadband noncollinear nonlinear optical phenomenon is, for the first time, observed in PPLN and CPPLN crystals, or in any other nonlinear crystals under such a transverse-setting configuration. These new multicolor transverse configurations enable the generation of the Raman–Nath emissions covering all the frequencies in the visible range at various diffraction angles. We believe that they surely will enrich the realm of nonlinear optics to create an ultrabroadband supercontinuum laser.

C. Principle of Transversely Phase-Matched UB-NRND Process

To explain the generation of ultrabroadband multi-order NRND processes in detail, we systematically consider, analyze, and summarize the transversely phase-matched conditions occurring in the PPLN and CPPLN samples, and illustrate them schematically in Fig. 4. The conventional monochromatic scheme of Raman–Nath patterns in a periodic nonlinear crystal like PPLN can be explained by the phase-matching geometry shown in Fig. 4(a). It turns out that the vectorial relation between the noncollinear interacting waves corresponds to the transverse-component matching, which can be expressed as

$$k_2 \sin\theta - G_m = 0, \qquad m = 0, \pm 1, \pm 2 \ldots. \tag{1}$$

In Eq. (1) and Fig. 4, k_2 is the wavevector of the SH signal in this NRND process, Δk is the wavevector mismatch, Λ is the poling period of the PPLN crystal with the single value of 6.96 μm, and m is the Raman–Nath diffraction order. $G_m = m(2\pi/\Lambda)$ is the mth-order RLV provided by the quadratic susceptibility tensor $\chi^{(2)}$ within the PPLN sample, which involves a series of fixed RLV lines, as displayed in Fig. 1(c). The parameter G_m is perpendicular to the fundamental light wavevector in this noncollinear scheme. For this simple QPM process, the transverse phase-matching between noncollinear interacting waves can be primitively satisfied by the nonlinear grating vector and then nonlinear diffraction behavior similar to diffraction of light by linear refractive index gratings will be realized.

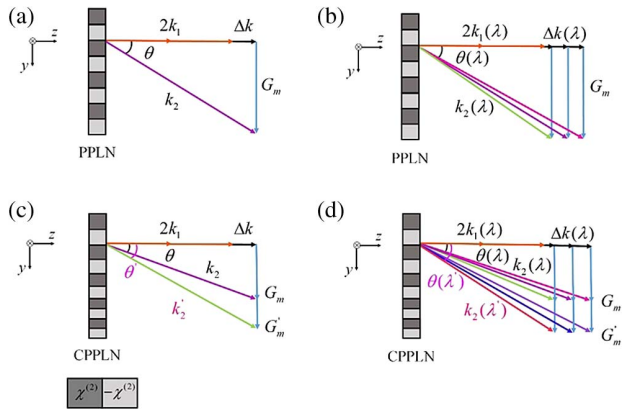

Fig. 4. Phase-matching diagram of NRND SHG process in the PPLN and CPPLN crystals. (a) Phase-matching diagram for monochromatic Raman–Nath SHG in the PPLN crystal via a single QPM 2nd NL process pumped by the monochromatic light. (b) Phase-matching diagram for multiple broadband Raman–Nath SHG in the PPLN crystal via synergic action of 2nd NL and 3rd NL for the high-peak-power femtosecond pump laser. (c) Phase-matching diagram for monochromatic Raman–Nath SHG in the CPPLN crystal via multiple QPM 2nd NL processes combined with the effect of broadband RLVs. (d) Phase-matching diagram for multiple ultrabroadband Raman–Nath SHG outputs in the CPPLN crystal via synergic action of 2nd NL and 3rd NL combined with multiple QPM interactions.

If the incident light is a high-peak-power ultrashort laser pulse with a broad operation bandwidth, the transverse vector condition of the NRND phase-matching should be described by a polychromic mechanism, which is represented by

$$k_2(\lambda)\sin\theta(\lambda) - G_m = 0, \qquad m = 0, \pm1, \pm2\ldots, \tag{2}$$

where $k_2(\lambda)$ represents the SH wavevectors of each spectral component at wavelength λ in the PPLN nonlinear crystal. The mth-order RLV G_m of the PPLN sample is represented as $G_m = m(2\pi/\Lambda)$, $\Lambda = 6.96$ μm. As clearly illustrated in Fig. 4(b), the recorded NRND pattern possesses multiple transverse phase matching due to the distinguished broad bandwidth of the ultrashort pump laser. In particular, 2nd NL and 3rd NL have played a synergistic role in the entire noncollinear Raman–Nath diffraction process. Rich spectral components of the interacting waves are added into the NRND process during the pump laser pulse proceeding within the nonlinear crystal. Consequently, multi-order beautiful and colorful NRND patterns encompassing wide wavelength ranges can be created in the periodic PPLN nonlinear crystal even with the compensation by just a single QPM transverse vector.

It is clear that a CPPLN crystal can offer much more flexible QPM schemes to satisfy various laser frequency conversion problems through the design of the modulation patterns and RLV spectra compared to a periodic PPLN crystal. Here, we apply and generalize this concept of broadband QPM interactions to noncollinear nonlinear diffraction, signifying that there will be multiple QPM transverse interactions in the NRND effect. The geometric representation of the QPM-NRND in the case of monochromatic pump radiation when passing through the CPPLN sample is summarized in Fig. 4(c), which shows that the Raman–Nath patterns can own broadening polychromatic processes with the participation of multiple RLVs. Supposing $\Lambda(y)$ represents the local period of modulation of the nonlinearity at position y inside the CPPLN crystal, which ranges from 24 to 14.8 μm, the corresponding mth-order RLVs band can be described by the segment $G_m \le G \le G'_m$, where G_m and G'_m correspond to the lower and upper ends of the mth-order RLV band, while $\Delta G_m = G'_m - G_m$ is the RLV bandwidth. As an approximation, the RLV band width can be estimated by a local period modulation model, which shows $G_m = m[2\pi/\Lambda(y)]$. The relevant mutative curves have been displayed in Fig. 1(d). Thus, we have

$$\begin{aligned} &k_2\sin\theta - G_m = 0,\\ &k'_2\sin\theta' - G'_m = 0, \qquad m = 0, \pm1, \pm2\ldots, \end{aligned} \tag{3}$$

for QPM-NRND. Here, θ and θ' correspond to the minimal and maximal diffraction angles for the mth-order QPM-NRND. One can find that a series of phase-matched Raman–Nath processes can be fully compensated with the contribution of the rich RLV bands offered by a CPPLN sample even under the pump of a monochromatic light, finally enabling the generation of single-color, broad-angle Raman–Nath patterns.

As we have discussed above, the most impressive ultrabroadband NRND phenomenon can be observed when multiple RLV bands are used in a system that possesses broadband natural spectral characteristics and superior third-order nonlinear effects, as clearly displayed in Fig. 3. These abundant and flexible transversely phase-matched processes corresponding to the newly named QPM-UB-NRND effect in a CPPLN sample yield strengthened smooth and balanced supercontinuum SH spectra, as adequately described in Figs. 3(b) and 3(c). In other words, the very broad spectrum of RLVs in the transverse direction enables the transverse phase-matching condition for a wide range of wavelengths to be satisfied, perfectly matching with the ultrabroadband nature of pump femtosecond pulse laser. Multiple QPM interactions between the CPPLN sample and the pump femtosecond laser (with the bandwidth enhanced by the 3rd NL effect) can be found geometrically using the brand new Raman–Nath phase-matching diagram shown in Fig. 4(d). Here, the more complicated, but more general, transverse geometric configuration responsible for QPM-UB-NRND radiation should be defined as

$$\begin{aligned} &k_2(\lambda)\sin\theta(\lambda) - G_m = 0,\\ &k'_2(\lambda)\sin\theta'(\lambda) - G'_m = 0, \quad m = 0, \pm1, \pm2\ldots. \end{aligned} \tag{4}$$

Equation (4) can be used as an efficient tool to describe the spectral and angular distribution of the generated NRND SH emissions from a CPPLN nonlinear crystal. Here, we can fully understand the enhanced ultrabroadband Raman–Nath effect that is associated with broad QPM vectors from the following two significant features. First, there exists several Raman–Nath phase-matched processes of multiple wavelengths corresponding to a single QPM interaction due to the distinguished 2nd NL and 3rd NL processes. This case is equivalent to the broadband Raman–Nath processes coming from a PPLN sample via the synergic action of 2nd NL and 3rd NL. Second, the CPPLN crystal offers a series of broad RLV bands in the transverse direction that enable multiple modified phase-matched transverse processes in the name of QPM-UB-NRND. Hence, these conditions allow some Raman–Nath emission bands to achieve more uniform supercontinuum spectra for a broad range of wavelengths compared to the QPM-UB-NRND scheme in a PPLN crystal. This expectation has been fully confirmed from the data comparatively displayed in Figs. 2 and 3. In other words, the broadening of the QPM spectrum in the CPPLN sample compared to a PPLN sample means more RLVs are available in the transverse direction, enabling multiple-fold fulfillment of the phase-matching conditions for the Raman–Nath process. In this case, the phase matching can be always satisfied for a broad range of incident wavelengths by selecting appropriate RLVs. Consequently, the NRND process in the CPPLN nonlinear crystal hints at a very promising means to accomplish efficient transversely quasi-phase-matched Raman–Nath SHG with greatly expanded wavelength ranges and to engineer multi-order supercontinuum generation. This scheme may in turn be harnessed to enhance and improve the high-precision supercontinuum spectroscopy techniques for applications in domain characterization and visualization of nonlinear microstructures.

D. NRND Angular Distribution and SH Conversion Efficiency

In the above, we have discussed the phase-matching interaction of a pump laser and an SH laser within the PPLN and CPPLN nonlinear crystals. In the following, we proceed to consider the output characteristics of an NRND SH beam from the nonlinear crystals; in particular, the diffraction angles of these multiple NRND SH beams. From the knowledge of general optics and diffractive optics, the external diffraction angle β is related to the internal angle θ by the refraction law and, more specifically, the condition of the transverse wavevector conservation law. It turns out that, according to Eq. (2), the external angle of the UB-NRND beams in the PPLN crystal are in the form of

$$\sin \beta_m(\lambda) = G_m/(2k_0) = m\lambda/\Lambda, \qquad m = 0, \pm 1, \pm 2\ldots, \tag{5}$$

while the angle in the CPPLN sample should be revised according to Eq. (4) as

$$\sin \beta_m(\lambda) = G_m/(2k_0) \approx m\lambda/\Lambda(y), \qquad m = 0, \pm 1, \pm 2\ldots, \tag{6}$$

where k_0 is the wavevector of the pump laser at 1300 nm and λ is the SH wavelength. According to Eq. (5), the angular position for the first-order NRND SH beam with a pump wavelength of 1300 nm in the periodic PPLN sample can be estimated to be 5.3587 deg relative to the central spot. As for the quasi-periodic CPPLN crystal, the angular distributions for the first-order NRND corresponding to the pump wavelength of 1300 nm should be closely related to the modulation period distribution, as shown in Fig. 5(a). One can see that the angular positions of Raman–Nath SH spots in the designed CPPLN crystal are basically inversely proportional to the domain poling period. It has been revealed that Raman–Nath diffraction is a global diffraction effect only dependent on the whole nonlinear microstructure, and the angular emissions of the Raman–Nath SH signals depend on the whole $\chi^{(2)}$ modulation rather than on locally partial periods [39]. For simplicity and without loss of generality, here we consider the numerical angular dependence of the mth diffraction order with the average poling period (i.e., the nonlinear grating period) for the CPPLN crystal. The average period of our CPPLN structure is 18.34 μm, which corresponds to an NRND angle of 2.0311 deg with the pump wavelength of 1300 nm. We have adopted this simplified model described in Eqs. (5) and (6) and calculated the angular curves of SH beams at different diffraction orders (in the left- and right-hand sides of the central spot) in both the PPLN and CPPLN samples for a quantitative illustration of the spatial distribution of the UB-NRND emission. The experimental data and calculation results are summarized in Fig. 5(b). Note that the angular emission is symmetric with respect to positive and negative diffraction orders and the radiation angle basically proportionally increases with increasing diffraction orders. Moreover, the experimental data and theoretical predictions are in good agreement with each other, indicating the efficiency of the simplified averaged-period model.

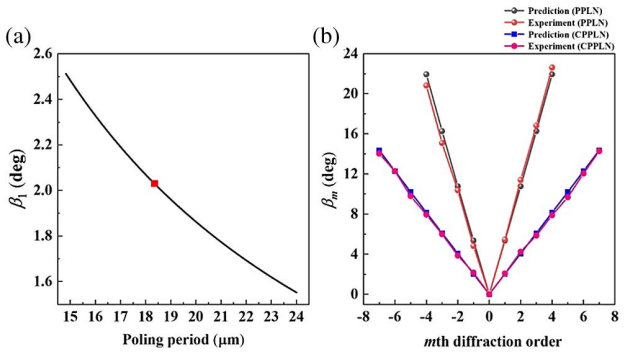

Fig. 5. Analysis of angular distribution of multiple-order NRND. (a) External angle of first-order UB-NRND in the CPPLN sample with different poling periods at the pump wavelength of 1300 nm. The red "square" mark represents the external angle corresponding to the average poling period of 18.34 μm. (b) Comparison between predicted and measured angular position for various NRND order parameters for the harmonics emissions from the PPLN and CPPLN samples at the pump wavelength of 1300 nm.

Finally, we analyze the energy conversion efficiency of this noncollinear ultrabroadband Raman–Nath diffraction effect through quantifying the diffraction power of each SH beam. An appropriate bandpass filter is chosen and placed before the power meter to eliminate the residual pump energy. In our experiment, the power of the pump laser is set to 60 mW. The estimated conversion efficiencies for various NRND orders are summarized and presented in Table 1. One can see that, for different diffraction orders of the nonlinear interactions, the conversion efficiencies of the UB-NRND effect in the CPPLN crystal are generally higher than in the PPLN crystal, which can be attributed to the contribution from multi-order RLV bands in CPPLN. Obviously, this quantitative conversion efficiency measurement corresponds well to the qualitative spectral analysis of the different Raman–Nath SH signals shown in Figs. 2 and 3. The optimal Raman–Nath SH conversion efficiency is up to 0.2% occurring in the UB-NRND process of CPPLN sample. Although this number is still not a high value compared to usual collinear QPM-SHG processes [4,5,36], it has already increased by a few orders of magnitude compared

Table 1. Measured UB-NRND Conversion Efficiency with Different Diffraction Orders in PPLN and CPPLN Crystals

Crystal	Negative Diffraction Order	UB-NRND Conversion Efficiency (%)	Positive Diffraction Order	UB-NRND Conversion Efficiency (%)
PPLN	−1	0.03412	+1	0.02970
	−2	0.09600	+2	0.05933
	−3	0.01750	+3	0.03017
	−4	0.00935	+4	0.01275
CPPLN	−1	0.05308	+1	0.05300
	−2	0.15667	+2	0.20167
	−3	0.04317	+3	0.02150
	−4	0.01017	+4	0.00800
	−5	0.00377	+5	0.00333
	−6	0.00143	+6	0.00112
	−7	0.00077	+7	0.00065

to the case of a conventional NRND scheme [24,28,40]. To the best of our knowledge, this is the most uniform and highest-efficiency Raman–Nath SH spectrum obtained to date from a single nonlinear crystal. Such a relatively considerable energy conversion efficiency of ultrabroadband Raman–Nath spectrum might enable the exact identification of the diffraction pattern variations and exhibit an excellent capability to detect domain structures and optical nonlinear susceptibilities within PPLN, CPPLN, and other domain modulation nonlinear microstructures in the platform of LN material.

3. CONCLUSIONS

In summary, we have realized efficient multi-order UB-NRND in both single PPLN and CPPLN nonlinear crystals upon illumination of a high-peak-power NIR ultrashort femtosecond pump laser perpendicular to the poling domain modulation direction. To fully characterize the emission performance of this UB-NRND effect, the angular distributions of SH radiations at different orders are experimentally studied and theoretically analyzed in detail. Meanwhile, the interaction efficiencies of the Raman–Nath interactions both in the PPLN and CPPLN samples are measured. The experimental results show that one can obtain a pretty visible supercontinuum white laser signal with a relatively uniform broad spectrum of wavelengths by harnessing the scheme of transversely phase-matched Raman–Nath diffraction in combination with an ultrabroadband QPM scheme. As a consequence, one can accomplish the UB-NRND effect in these nonlinear microstructures.

On the other hand, the ultrabroadband Raman–Nath spectra in the CPPLN sample show prominent features of markedly enhanced and smooth averaged spectra in the entire visible wavelength ranges compared to the PPLN sample. The success is attributed to several factors. First, the natural broad wavelength band of an ultrashort pump laser is necessary to initiate broadband Raman–Nath diffraction. Second, the dominating 3rd NL effects originating from the high-peak-power pump laser help to create a series of new spectral components accompanying the pump laser, which can further expand the bandwidth of the output broadband NRND signals. Third, the implementation of the conversional QPM technique inherent in these nonlinear microstructures can excellently fit the process of NRND and overcome the severe non-phase-matched limitation inherent in bulky nonlinear crystals. One can see that multiple QPM bands enable more channels of broadband Raman–Nath diffractions, leading to a noteworthy enhancement of SHG outputs and a balance of second-harmonic wavelengths between NRND orders, and accomplishing the QPM-UB-NRND effects. All these three physical processes and mechanisms make a major contribution to the Raman–Nath SHG, work together, and create gorgeous multiple-order broadband radiation patterns in the visible band.

Additionally, it is worth emphasizing that the generated SH diffraction via the NRND process mainly originates from the enhanced nonlinearity of domain wall regions in the nonlinear ferroelectric crystal [29], and will not be observable in a bare LN crystal. Meanwhile, a change in the period of modulation upon the nonlinear susceptibility should exert influence on the width of the SH angular spectrum. Hence, when varying the parameters of the poling microstructure and femtosecond pump laser, the spatial and spectral characteristics of SH emitted waves would be modulated in a broad range. Consequently, this new strategy that allows for a supercontinuum Raman–Nath diffraction spectrum will not only critically enrich the physical understanding of the Raman–Nath effect in nonlinear microstructures, but also will add a sufficient degree of freedom in the realm of nonlinear optics to realize ultrabroadband supercontinuum lasers. More importantly, due to the ultrabroadband nature and considerable energy conversion efficiency, we believe this NRND scheme will bring better techniques and tools for applications ranging from ultrashort pulse characterization and nondestructive identification of domain structures to accurate parameter monitoring of second- and third-order nonlinear susceptibilities within solid-state nonlinear microstructured materials.

Funding. National Natural Science Foundation of China (11974119); Science and Technology Project of Guangdong (2020B010190001); Guangdong Innovative and Entrepreneurial Research Team Program (2016ZT06C594); National Key Research and Development Program of China (2018YFA0306200); Natural Science Foundation of Guangdong Province of China (2019A1515011605).

Disclosures. The authors declare no conflicts of interest.

Data Availability. Data underlying the results presented in this paper are not publicly available at this time but may be obtained from the authors upon reasonable request.

REFERENCES

1. P. A. Franken and J. F. Ward, "Optical harmonics and nonlinear phenomena," Rev. Mod. Phys. **35**, 23–39 (1963).
2. M. M. Fejer, G. A. Magel, D. H. Jundt, and R. L. Byer, "Quasi-phase-matched second harmonic generation: tuning and tolerances," IEEE J. Quantum Electron. **28**, 2631–2654 (1992).
3. B. Q. Ma, T. Wang, Y. Sheng, P. G. Ni, Y. Q. Wang, B. Y. Cheng, and D. Z. Zhang, "Quasiphase matched harmonic generation in a two-dimensional octagonal photonic superlattice," Appl. Phys. Lett. **87**, 251103 (2005).
4. B. Q. Chen, M. L. Ren, R. J. Liu, C. Zhang, Y. Sheng, B. Q. Ma, and Z. Y. Li, "Simultaneous broadband generation of second and third harmonics from chirped nonlinear photonic crystals," Light Sci. Appl. **3**, e189 (2014).
5. B. Q. Chen, C. Zhang, C. Y. Hu, R. J. Liu, and Z. Y. Li, "High-efficiency broadband high-harmonic generation from a single quasi-phase-matching nonlinear crystal," Phys. Rev. Lett. **115**, 083902 (2015).
6. B. Q. Chen, L. H. Hong, C. Y. Hu, and Z. Y. Li, "Engineering quadratic nonlinear photonic crystals for frequency conversion of lasers," J. Opt. **20**, 034009 (2018).
7. M. L. Ren, D. L. Ma, and Z. Y. Li, "Experimental demonstration of super quasi-phase matching in nonlinear photonic crystal," Opt. Lett. **36**, 3696–3698 (2011).
8. I. Freund, "Nonlinear diffraction," Phys. Rev. Lett. **21**, 1404–1406 (1968).
9. X. Fang, D. Wei, D. Liu, W. Zhong, R. Ni, Z. Chen, X. Hu, Y. Zhang, S. N. Zhu, and M. Xiao, "Multiple copies of orbital angular momentum states through second-harmonic generation in a two-dimensional periodically poled $LiTaO_3$ crystal," Appl. Phys. Lett. **107**, 161102 (2015).
10. N. G. R. Broderick, R. T. Bratfalean, T. M. Monro, D. J. Richardson, and C. M. de Sterke, "Temperature and wavelength tuning of second-, third-, and fourth-harmonic generation in a two-dimensional

hexagonally poled nonlinear crystal," J. Opt. Soc. Am. B **19**, 2263–2272 (2002).
11. S. M. Saltiel, D. N. Neshev, R. Fischer, W. Krolikowski, A. Arie, and Y. S. Kivshar, "Generation of second-harmonic Bessel beams by transverse phase-matching in annular periodically poled structures," Jpn. J. Appl. Phys. **47**, 6777–6783 (2008).
12. Y. Zhang, Z. D. Gao, Z. Qi, S. N. Zhu, and N. B. Ming, "Nonlinear Čerenkov radiation in nonlinear photonic crystal waveguides," Phys. Rev. Lett. **100**, 163904 (2008).
13. N. An, H. Ren, Y. Zheng, X. Deng, and X. Chen, "Cherenkov high-order harmonic generation by multistep cascading in $\chi^{(2)}$ nonlinear photonic crystal," Appl. Phys. Lett. **100**, 221103 (2012).
14. H. X. Li, S. Y. Mu, P. Xu, M. L. Zhong, C. D. Chen, X. P. Hu, W. N. Cui, and S. N. Zhu, "Multicolor Čerenkov conical beams generation by cascaded-$\chi^{(2)}$ processes in radially poled nonlinear photonic crystals," Appl. Phys. Lett. **100**, 101101 (2012).
15. L. H. Peng, C. C. Hsu, and Y. C. Shih, "Second-harmonic green generation from two-dimensional $\chi^{(2)}$ nonlinear photonic crystal with orthorhombic lattice structure," Appl. Phys. Lett. **83**, 3447–3449 (2003).
16. Y. Sheng, J. H. Dou, B. Q. Ma, B. Y. Cheng, and D. Z. Zhang, "Broadband efficient second harmonic generation in media with a short-range order," Appl. Phys. Lett. **91**, 011101 (2007)
17. D. D. Liu, D. Z. Wei, M. Gu, Y. Zhang, X. P. Hu, M. Xiao, and P. Han, "Evolution of the nonlinear Raman–Nath diffraction from near field to far field," Opt. Lett. **43**, 3168–3171 (2018).
18. A. M. Vyunishev, V. V. Slabko, I. S. Baturin, A. R. Akhmatkhanov, and V. Ya. Shur, "Nonlinear Raman–Nath diffraction of femtosecond laser pulses," Opt. Lett. **39**, 4231–4234 (2014).
19. A. M. Vyunishev and A. S. Chirkin, "Multiple quasi-phase-matching in nonlinear Raman–Nath diffraction," Opt. Lett. **40**, 1314–1317 (2015).
20. A. M. Vyunishev, V. G. Arkhipkin, V. V. Slabko, I. S. Baturin, A. R. Akhmatkhanov, V. Y. Shur, and A. S. Chirkin, "Nonlinear Raman–Nath diffraction of femtosecond laser pulses in a 2D nonlinear photonic crystal," Opt. Lett. **40**, 4002–4005 (2015).
21. Y. Sheng, W. Wang, R. Shiloh, V. Roppo, A. Arie, and W. Krolikowski, "Third-harmonic generation via nonlinear Raman–Nath diffraction in nonlinear photonic crystal," Opt. Lett. **36**, 3266–3268 (2011).
22. S. M. Saltiel, D. N. Neshev, W. Krolikowski, A. Arie, O. Bang, and Y. S. Kivshar, "Multiorder nonlinear diffraction in frequency doubling processes," Opt. Lett. **34**, 848–850 (2009).
23. S. M. Saltiel, D. N. Neshev, R. Fischer, W. Krolikowski, A. Arie, and Y. S. Kivshar, "Generation of second-harmonic conical waves via nonlinear Bragg diffraction," Phys. Rev. Lett. **100**, 103902 (2008).
24. S. M. Saltiel, D. N. Neshev, W. Krolikowski, N. Voloch-Bloch, A. Arie, O. Bang, and Y. S. Kivshar, "Nonlinear diffraction from a virtual beam," Phys. Rev. Lett. **104**, 083902 (2010).
25. A. Shapira and A. Arie, "Phase-matched nonlinear diffraction," Opt. Lett. **36**, 1933–1935 (2011).
26. Y. Sheng, Q. Kong, W. J. Wang, K. Kalinowski, and W. Krolikowski, "Theoretical investigations of nonlinear Raman–Nath diffraction in the frequency doubling process," J. Phys. B **45**, 055401 (2012).
27. X. G. Wang, X. H. Zhao, Y. L. Zheng, and X. F. Chen, "Theoretical study on second-harmonic generation in two-dimensional nonlinear photonic crystals," Appl. Opt. **56**, 750–754 (2017).
28. P. Karpinski, X. Chen, V. Shvedov, C. Hnatovsky, A. Grisard, E. Lallier, B. Luther-Davies, W. Krolikowski, and Y. Sheng, "Nonlinear diffraction in orientation-patterned semiconductors," Opt. Express **23**, 14903–14912 (2015).
29. X. W. Deng, H. J. Ren, H. Y. Lao, and X. F. Chen, "Research on Cherenkov second-harmonic generation in periodically poled lithium niobate by femtosecond pulses," J. Opt. Soc. Am. B **27**, 1475–1480 (2010).
30. X. W. Deng and X. F. Chen, "Domain wall characterization in ferroelectrics by using localized nonlinearities," Opt. Express **18**, 15597–15602 (2010).
31. K. Kalinowski, P. Roedig, Y. Sheng, M. Ayoub, J. Imbrock, C. Denz, and W. Krolikowski, "Enhanced Čerenkov second-harmonic emission in nonlinear photonic structures," Opt. Lett. **37**, 1832–1834 (2012).
32. A. Piskarskas, V. Smilgevicius, A. Stabinis, V. Jarutis, V. Pasiskevicius, S. Wang, J. Tellefsen, and F. Laurell, "Noncollinear second-harmonic generation in periodically poled $KTiOPO_4$ excited by the Bessel beam," Opt. Lett. **24**, 1053–1055 (1999).
33. M. Nakamura, M. Sugihara, M. Kotoh, H. Taniguchi, and K. Tadatomo, "Quasi-phase-matched optical parametric oscillator using periodically poled MgO-doped $LiNbO_3$ crystal," Jpn. J. Appl. Phys. **38**, L1234–L1236 (1999).
34. H. Ishizuki, T. Taira, S. Kurimura, J. H. Ro, and M. Cha, "Periodic poling in 3-mm-thick MgO:$LiNbO_3$ crystals," Jpn. J. Appl. Phys. **42**, L108–L110 (2003).
35. L. H. Peng, Y. C. Zhang, and Y. C. Lin, "Zinc oxide doping effects in polarization switching of lithium niobate," Appl. Phys. Lett. **78**, 4–6 (2004).
36. M. Nakamura, T. Tsunekawa, H. Taniguchi, and K. Tadamoto, "Optical parametric oscillator on 1-mm-thick periodically poled $LiNbO_3$ with 29 mm interaction length," Jpn. J. Appl. Phys. **38**, L1175–L1177 (1999).
37. B. Q. Chen, L. H. Hong, C. Y. Hu, and Z. Y. Li, "White laser realized via synergic second-and third-order nonlinearities," Research **2021**, 1539730 (2021).
38. H. Jang, G. Strömqvist, V. Pasiskeviciu, and C. Canalias, "Control of forward stimulated polariton scattering in periodically-poled KTP crystals," Opt. Express **21**, 27277–27283 (2013).
39. Y. P. Chen, W. R. Dang, Y. L. Zheng, X. F. Chen, and X. W. Deng, "Spatial modulation of second-harmonic generation via nonlinear Raman–Nath diffraction in an aperiodically poled lithium tantalite," Opt. Lett. **38**, 2298–2300 (2013).
40. J. Trull, S. Saltiel, V. Roppo, C. Cojocaru, D. Dumay, W. Krolikowski, D. N. Neshev, R. Vilaseca, K. Staliunas, and Y. S. Kivshar, "Characterization of femtosecond pulses via transverse second-harmonic generation in random nonlinear media," Appl. Phys. B **95**, 609–615 (2009).